Twist-angle transferable continuum model and second flat Chern band in twisted MoTe$_2$ and WSe$_2$

Xiao-Wei Zhang,[1] Kaijie Yang,[1] Chong Wang,[1] Xiaoyu Liu,[1] Ting Cao,[1, *] and Di Xiao[1, 2, 3, †]

[1]*Department of Materials Science and Engineering,*
University of Washington, Seattle, Washington 98195, USA
[2]*Department of Physics, University of Washington, Seattle, Washington 98195, USA*
[3]*Pacific Northwest National Laboratory, Richland, Washington 99354, USA*

We develop a twist-angle transferable continuum model for twisted transition metal dichalcogenide (tTMD) homobilayers, using tMoTe$_2$ and tWSe$_2$ as examples. All model parameters are extracted from density functional theory (DFT) calculations at a single twist angle (3.89°) and monolayer data. Our model captures both lattice relaxation effects and the long-range behavior of piezoelectric and ferroelectric potentials. Leveraging lattice relaxations obtained via machine learning force fields (MLFFs), the model can be efficiently transferred to other twist angles without requiring additional DFT calculations. It accurately reproduces the DFT band dispersions and quantum geometries across a wide range of twist angles. Furthermore, our model reveals that a second flat Chern band arises near 2° when the interlayer potential difference becomes comparable to the interlayer tunneling. This continuum model provides a clear understanding and starting point for engineering novel electronic phases in moiré TMDs through twist angles and lattice relaxations.

In recent years, substantial experimental progress has been made in observing novel electronic phases due to the interplay between topology and correlations in R-type moiré TMD homobilayers [1–15], including zero-field fractional Chern insulators [1–4] and superconductivity [14, 15]. Theoretically, continuum models are widely used as a single-particle starting point for studying these phases. However, constructing such models remains challenging due to significant lattice relaxation effects. Unlike twisted bilayer graphene, R-type tTMDs permit moiré ferroelectricity and piezoelectricity, arising from local inversion symmetry breaking. Prior DFT studies have demonstrated that the twist-angle dependent competition between these two polarizations plays a crucial role in shaping moiré band structures and quantum geometries [16–19]. Notably, multiple flat bands with Chern number $C = 1$ were first predicted near 2° in tMoTe$_2$ [16] and signatures of non-Abelian states were later proposed at half-filling of the second flat band [20–24]. However, the physical origin of the second flat Chern band is still unclear based on the current continuum models.

In developing the continuum model, an initial version was constructed using first-harmonic intralayer potentials and interlayer tunneling, with parameters obtained by fitting DFT band structures at various local stackings [25]. However, this model fails to accurately describe the system due to the absence of moiré-scale lattice relaxation [19]. Subsequent approaches have involved parameterizing the continuum model by fitting large-scale DFT moiré band structures and incorporating higher harmonics to account for relaxations [18–20, 22]. Nevertheless, such fitting procedures introduce inconsistencies across twist angles due to the vast parameter space involved. Alternatively, some efforts have focused on incorporating additional terms—such as those accounting for corrugations and piezoelectric effects—directly into the model [26, 27]. Yet, the resulting models are still not accurate due to the incomplete treatment of lattice relaxation effects and long-range ferroelectric potentials.

More recently, a precise parameterization method has been developed, which projects the DFT Hamiltonian directly onto the continuum model basis without the need for fitting [28]. Although this approach is exact, it remains computationally expensive, as large-scale DFT calculations are required for each twist angle. Therefore, striking a balance between efficiency and accuracy remains challenging.

In this work, we develop a twist-angle transferable continuum model for R-type tWSe$_2$ and tMoTe$_2$. The model comprehensively captures lattice relaxation effects and the long-range behavior of piezoelectric and ferroelectric electrostatic potentials, based on spatially varying interlayer distance $d(\boldsymbol{r})$ and in-plane atomic displacement field $\boldsymbol{u}(\boldsymbol{r})$. The model is parameterized at a single twist angle (3.89°) by fitting large-scale DFT band structures, supplemented with monolayer data. With lattice relaxations provided by MLFFs, the model can be efficiently transferred to arbitrary twist angles without requiring additional DFT calculations. Its accuracy is validated by reproducing DFT band dispersions and quantum geometries across the 2°–5° range. By analyzing the twist-angle dependence of the moiré potentials generated by the model, we uncover the origin of a second flat Chern band emerging near 2° in both systems. This feature arises because the interlayer potential differences and interlayer tunneling become comparable as θ varies. The developed continuum model is generalizable to other moiré TMD systems and offers a powerful basis for engineering novel electronic phases through twist angle tuning, strain, and pressure.

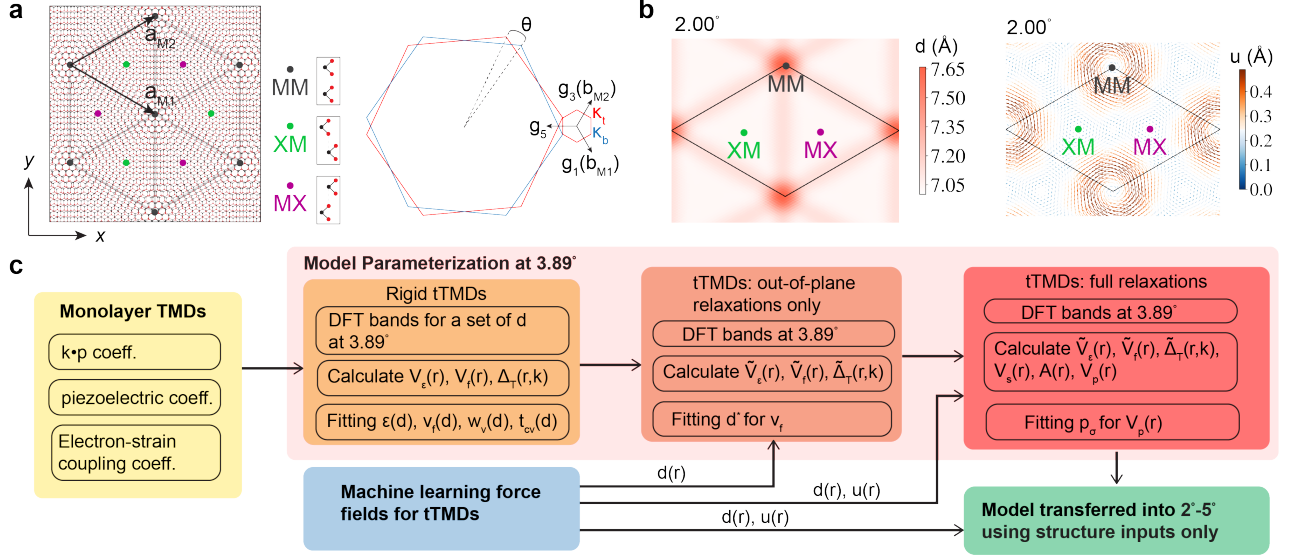We begin by incorporating lattice relaxation and long-

FIG. 1. **Moiré superlattice, lattice relaxations, and model parameterization a**, schematic illustration of the moiré superlattice and the moiré Brillouin zone. The three high-symmetry stackings—MM, XM, and MX—are indicated. **b**, interlayer distance (ILD) distribution (left) and top-layer in-plane atomic displacements (right) for $2.00°$ tMoTe$_2$. Colors represent the magnitude of in-plane displacements, while arrows indicate their directions. **c**, workflow for model parameterization using DFT calculations and subsequent model predictions incorporating moiré lattice relaxations obtained from MLFFs.

range polarization effects into our model. In R-type TMDs, the lack of inversion symmetry in monolayer TMDs allows intralayer piezoelectric polarizations induced by strain fields in each layer [29]. Because the two layers have opposite atomic displacements and the same piezoelectric coefficients, the piezoelectric polarizations can cause a vertical potential drop across the bilayer [16, 26, 30]. Moreover, the inversion symmetry breaking at local stackings in R-type tTMDs permits moiré ferroelectric polarizations [7, 31, 32]. These polarization charges generate long-range electrostatic potentials. While prior studies have considered the long-range nature of the piezoelectric potential, the ferroelectric po-

tential has typically been treated as a local stacking-dependent effect [26]. Here, we first analyze a rigidly twisted moiré superlattice to capture the long-range ferroelectric potential, and then incorporate the effects of lattice relaxation.

Rigid lattice.—In the rigid lattice, the top layer is rotated by θ relative to the bottom layer and lattice relaxations are excluded [Fig. 1(a)]. As a result, the local shift vector between the two layers is expressed as $\boldsymbol{r}_0 = \theta\hat{z}\times\boldsymbol{r}$. In this case, although the piezoelectric polarizations vanish, moiré ferroelectric polarizations still exist. To fit the bands, we begin with the $\boldsymbol{k}\cdot\boldsymbol{p}$ continuum model for the spin-up K valley [25, 33, 34]:

$$\mathcal{H}_{K\uparrow} = \begin{pmatrix} -\frac{(\boldsymbol{p}-\hbar\boldsymbol{\kappa}_b)^2}{2m^*} + h_{\text{kin,b}}^{h.o.} + V_\varepsilon(\boldsymbol{r}) - \frac{V_f(\boldsymbol{r})}{2} & \Delta_T(\boldsymbol{r},\boldsymbol{k}) \\ \Delta_T^\dagger(\boldsymbol{r},\boldsymbol{k}) & -\frac{(\boldsymbol{p}-\hbar\boldsymbol{\kappa}_t)^2}{2m^*} + h_{\text{kin,t}}^{h.o.} + V_\varepsilon(\boldsymbol{r}) + \frac{V_f(\boldsymbol{r})}{2} \end{pmatrix}. \tag{1}$$

The spin-down K'-valley Hamiltonian can be obtained through the time-reversal operation. Here, $\boldsymbol{\kappa}_b$ and $\boldsymbol{\kappa}_t$ denote the rotated K point of the bottom and top layer, respectively. The layer-symmetric potentials V_ε and ferroelectric potential V_f can be expanded using the first-harmonic approximation,

$$V_\varepsilon(\boldsymbol{r}) = \varepsilon(d) \sum_{j=1,3,5}^{1s} \cos(\boldsymbol{g}_j \cdot \boldsymbol{r}), \tag{2}$$

and

$$V_f(\boldsymbol{r}) = v_f(d,\theta) \sum_{j=1,3,5}^{1s} \sin(\boldsymbol{g}_j \cdot \boldsymbol{r}). \tag{3}$$

Here, $\boldsymbol{g}_j$ denotes the moiré reciprocal lattice vector (as defined in Fig. 1(a)) and d is the interlayer distance. The

interlayer tunneling is given by

$$\Delta_T(\boldsymbol{r}, \boldsymbol{k}) = T_v(\boldsymbol{r}) - \hbar v_F |\boldsymbol{k} - \boldsymbol{k}_b| e^{i(\theta_k + \theta/2)} T_{cv}(\boldsymbol{r})/E_g$$
$$- \hbar v_F T_{vc}(\boldsymbol{r}) |\boldsymbol{k} - \boldsymbol{\kappa}_t| e^{-i(\theta_k - \theta/2)}/E_g. \quad (4)$$

Here, E_g and v_F denote the band gap and Fermi velocity of the monolayer TMD, respectively. The three interlayer tunneling terms, T_v, T_{cv}, and T_{vc}, are all expanded in the first-harmonic form, i.e.

$$T_{n_j}(\boldsymbol{r}) = w_{n_j}(d)(1 + e^{-i2\pi j/3} e^{-i\boldsymbol{g}_3 \cdot \boldsymbol{r}} + e^{i2\pi j/3} e^{i\boldsymbol{g}_1 \cdot \boldsymbol{r}}), \quad (5)$$

where $j = \{0, 1, 2\}$, $n_j = \{v, cv, vc\}$, and v/c denote the valence/conduction band.

Compared to the previous continuum models [25–27], our formulation in Eq. 1 introduces three improvements. First, we take into account the long-range nature of the ferroelectric potential V_f. Although the ferroelectric potential itself is long-range, it originates from localized charge transfer around the MX/XM regions. By solving the Poisson equation, we derive an analytical expression for the amplitude of V_f:

$$v_f(\theta, d) = \tilde{v}_f(d)(1 - e^{-gd})/(gd). \quad (6)$$

Here, g is the modulus of the first-shell moiré reciprocal lattice vector. Including this long-range behavior is crucial for ensuring the model's transferability across different twist angles. Second, we incorporate intralayer higher-order kinetic terms, denoted as $h_{kin,b/t}^{h.o.}$. Third, we incorporate high order momentum dependence in the interlayer tunneling by including tunneling processes between the conduction and valence bands. Notably, the second and third terms in Eq. 4 correspond to the layer-orbit coupling term introduced in Ref. [35].

To ensure the model's transferability with respect to θ, it is essential to analyze the θ-dependence of various terms. First, the kinetic energy parameters are assumed to be independent of θ. Second, the ferroelectric potential amplitude v_f exhibits an explicit θ-dependence through the function $g(\theta)$ in Eq. 6. Third, since the interlayer tunneling is short-ranged in real space, we assume the corresponding amplitudes w_v, w_{cv}, and w_{vc} are independent of θ. Lastly, the term V_ε represents an average potential between the layers arising from local stacking variations, and we likewise assume the parameter ε is independent of θ. Further details regarding Eq. 1 can be found in the Supplementary Note 3.

Relaxed lattice.— We next incorporate lattice relaxation effects into the continuum model. Figure 1(b) illustrates the interlayer distance distribution and in-plane atomic displacements for $2.00°$ tMoTe$_2$. Consistent with previous studies [13, 16], triangular domain formations are observed. These significant corrugations render the parameters ε, w_v, and w_{cv} spatially dependent through substitution with the spatially varying interlayer distance $d(\boldsymbol{r})$. However, for the parameter $\tilde{v}_f$, the spatial variation of $d(\boldsymbol{r})$ complicates the solution of the Poisson equation. To retain analytical tractability, we introduce an effective interlayer distance, d^*, obtained as the spatial average of $d(\boldsymbol{r})$. Details regarding the determination of d^* are provided in Supplementary Note 2.

The in-plane relaxations introduce three distinct effects. First, the local shift vector $\boldsymbol{r}_0$ is modified as follows

$$\boldsymbol{r}_0 = \theta \hat{z} \times \boldsymbol{r} + \boldsymbol{u}_t - \boldsymbol{u}_b, \quad (7)$$

where $\boldsymbol{u}_t$ and $\boldsymbol{u}_b$ denote the atomic displacements of the top and bottom layers, respectively [36]. Second, the strain field induces scalar and pseudo-vector potentials, given by $V_s(\boldsymbol{r}) = \zeta_1(u_{xx} + u_{yy})$ and $\boldsymbol{A}(\boldsymbol{r}) = -(\hbar\zeta_2)/(ea)(u_{xx} - u_{yy}, -2u_{xy})$ [37, 38]. Here, a is the lattice constant of the monolayer TMD, e is the elementary charge, and ζ_1 and ζ_2 are $\boldsymbol{k} \cdot \boldsymbol{p}$ parameters for a strained monolayer TMD. Third, the strain gradient induces piezoelectric charge densities in each layer, expressed as $\rho_{\text{piezo}} = \tilde{e}_{11}[2\partial_x u_{xy} + \partial_y(u_{xx} - u_{yy})]$, which generate piezoelectric potentials $V_{p,t/b}(\boldsymbol{r})$ [26, 30]. Similar to V_f, the long-range nature of $V_{p,t/b}$ is captured by solving the Poisson equation, with the expressions provided in Supplementary Note 2. To account for screening effects from the TMD layers themselves, we introduce a spatially uniform screening factor p_σ.

The total Hamiltonian incorporating lattice relaxation effects can now be written as

$$\tilde{\mathcal{H}}_{K\uparrow} = \begin{pmatrix} -\frac{(\boldsymbol{p} - \hbar\boldsymbol{\kappa}_b + e\boldsymbol{A}_b)^2}{2m^*} + h_{\text{kin,b}}^{h.o.} + \Delta_b(\boldsymbol{r}) & \tilde{\Delta}_T(\boldsymbol{r}, \boldsymbol{k}) \\ \tilde{\Delta}_T^\dagger(\boldsymbol{r}, \boldsymbol{k}) & -\frac{(\boldsymbol{p} - \hbar\boldsymbol{\kappa}_t + e\boldsymbol{A}_t)^2}{2m^*} + h_{\text{kin,t}}^{h.o.} + \Delta_t(\boldsymbol{r}) \end{pmatrix}. \quad (8)$$

Here, Δ_b and Δ_t denote the bottom and top-layer potentials, respectively, i.e.

$$\Delta_b(\boldsymbol{r}) = \tilde{V}_\varepsilon(\boldsymbol{r}) - \tilde{V}_f(\boldsymbol{r})/2 + V_{p,b}(\boldsymbol{r}) + V_{s,b}(\boldsymbol{r}) \quad (9)$$

and

$$\Delta_t(\boldsymbol{r}) = \tilde{V}_\varepsilon(\boldsymbol{r}) + \tilde{V}_f(\boldsymbol{r})/2 + V_{p,t}(\boldsymbol{r}) + V_{s,t}(\boldsymbol{r}). \quad (10)$$

Note that the formulations of $\tilde{V}_\varepsilon$, $\tilde{V}_f$, and $\tilde{\Delta}_T$ slightly differ from their definitions in Eqs. 2–4 due to the modi-
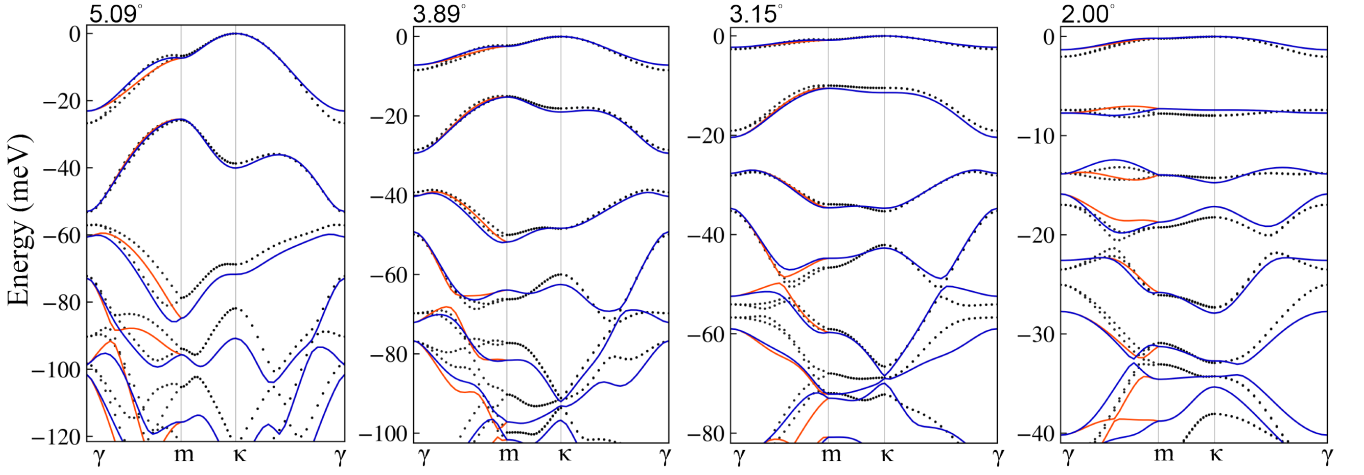
FIG. 2. **Moiré band structures.** Comparison of band dispersions between the continuum model and DFT for 5.08°, 3.89°, 3.15°, and 2.00° tMoTe$_2$. Black dots correspond to the DFT results, and red (blue) lines denote the spin-up (spin-down) bands at the K (K') valley obtained from the continuum model. All continuum model parameters are fitted at 3.89°.
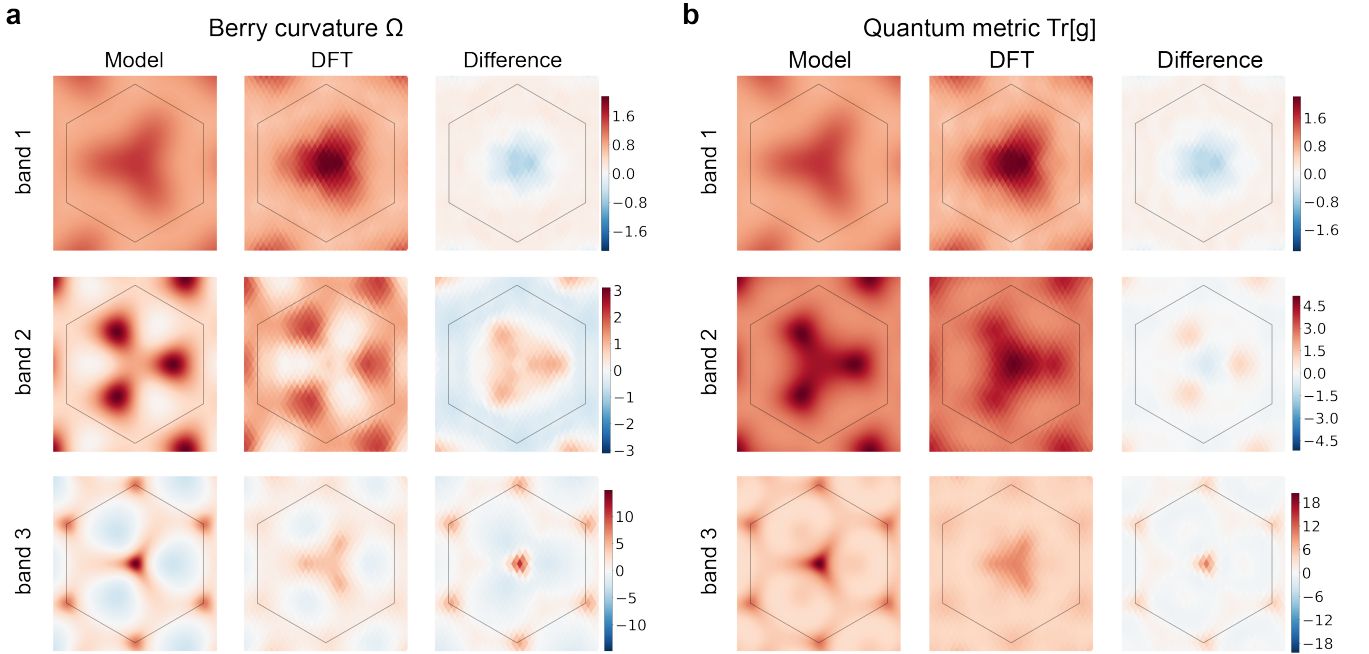

FIG. 3. **Distributions of Berry curvature and quantum metric of 2.00° tMoTe$_2$.** **a**, Berry curvature (Ω) distributions in the first mBZ for the first three K-valley moiré bands, obtained from the continuum model (left), DFT-based Wannier interpolations (middle), and their differences (right). **b**, similar to **a**, but shows the distribution of the trace of the quantum metric, Tr(g), in the mBZ. Ω and Tr(g) are multiplied by the mBZ area and divided by 2π. The black hexagon outlines the first mBZ.

fications of local shift vector as shown in Eq. 7 (see Supplementary Note 3). Since all model parameters can be extracted from a single twist angle (in practice, 3.89° is selected for its computational efficiency and experimental relevance) along with monolayer TMD inputs, the continuum model at arbitrary twist angles can be constructed directly from the moiré structural information obtained through MLFFs, without requiring additional

large-scale DFT calculations. Equation 8 represents the central result of this work.

We now briefly outline the parameterization workflow of the continuum model, as illustrated in Fig. 1(c). First, we compute the $\boldsymbol{k} \cdot \boldsymbol{p}$ coefficients, piezoelectric coefficient $\tilde{e}_{11}$, and electron-strain coupling coefficients ξ_1 and ξ_2 for monolayer TMDs. Next, we extract $\varepsilon(d)$, $\tilde{v}_f(d)$, $w_v(d)$, and $w_{cv}(d)$ in Eqs. 2–5 by fitting DFT moiré bands over
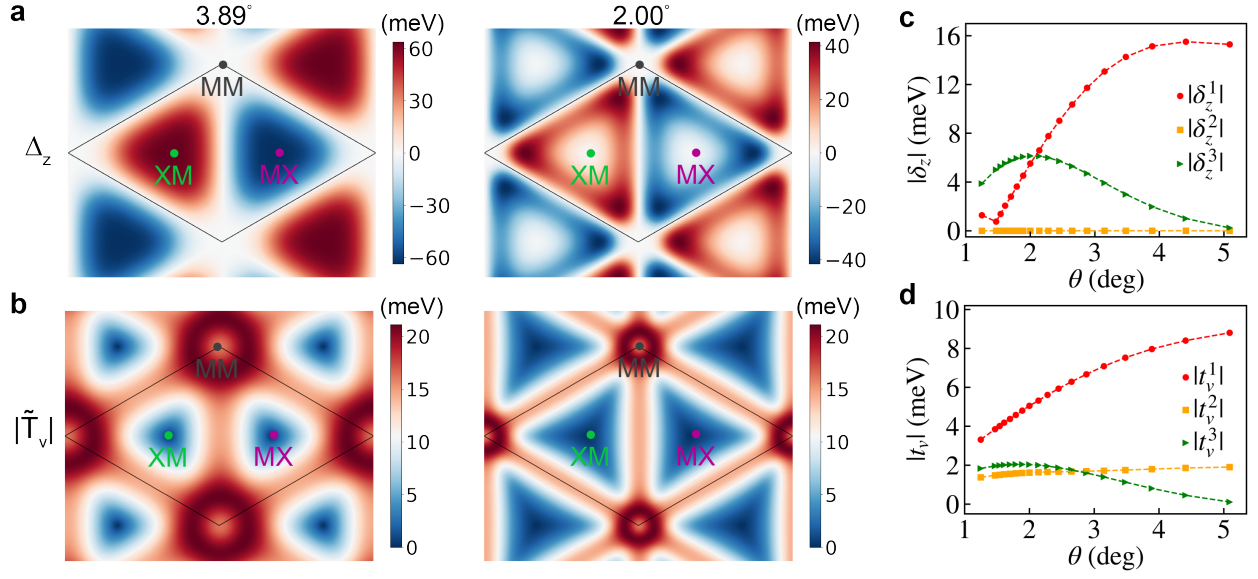
FIG. 4. **Twist-angle dependence of moiré potentials in tMoTe$_2$. a-b**, real-space distributions of $\Delta_z(\boldsymbol{r})$ and $|\tilde{T}_v(\boldsymbol{r})|$, at 3.89° and 2.00°. The black parallelogram outlines a moiré unit cell. **c–d**, twist-angle dependence of the modulus of the Fourier components for $\Delta_z(\boldsymbol{r})$ and $\tilde{T}_v(\boldsymbol{r})$. δ_z^i and t_v^i denote the ith-shell harmonic contribution for $\Delta_z(\boldsymbol{r})$ and $\tilde{T}_v(\boldsymbol{r})$, respectively.

a series of interlayer distances at 3.89°. The effective interlayer distance d^* for $\tilde{V}_f$ is then determined by fitting DFT bands computed with out-of-plane relaxations only. Subsequently, with both in-plane and out-of-plane relaxations included, we determine the screening factor p_σ for the piezoelectric potential $V_{p,t/b}$ by further fitting to DFT moiré bands at 3.89°. Additional details of the parameterization are provided in Supplementary Note 2, where all the model parameters are tabulated.

Model validation and transferability.—Next, we validate the continuum model by comparing its predictions with DFT results. As shown in Fig. 2, moiré band structures from the model are benchmarked against DFT calculations across a range of twist angles from 2.00° to 5.08°. At 3.89°, where the model parameters are fitted, excellent agreement is observed for at least the top three valence moiré bands in each valley. In addition, the model accurately captures the valley splittings along the γ–m path for the top bands, primarily due to T_{cv} (T_{vc}) and trigonal warping. Notably, the model maintains good agreement with DFT across the full twist angle range. The generalizability of the continuum model is further demonstrated for tWSe$_2$, as shown in Supplementary Note 2.

To further assess the model, we compare its quantum geometries with those obtained from Wannier-interpolated DFT calculations. In Fig. 3(a) and (b), we show the distributions of Berry curvature Ω and the trace of the quantum metric $\mathrm{Tr}(g)$ for the first three K-valley moiré bands at 2.00° for tMoTe$_2$. The model successfully reproduces the momentum dependence of both quantities, as evidenced by the overall small differences shown

in the right columns of 3(a) and (b). Integration over the moiré Brillouin zone yields identical Chern numbers $(+1, +1, +1)$ for both the continuum model and DFT results. Furthermore, the integrated values of $\mathrm{Tr}(g)$ from the model—$(1.04, 3.13, 5.26)$—closely match those from the DFT—$(1.04, 3.09, 5.11)$ [24].

Origin of second flat Chern band.— The twist-angle transferability of the continuum model enables us to investigate the physical origin of the second flat Chern band emerging around 2.00°, a feature first predicted by DFT calculations for tMoTe$_2$ and tWSe$_2$ [16] (also see Supplementary Note 1). Through a pertubative analysis of the energy and C_3 eigenvales at the γ and κ points, we find that the main reason lies in the twist-angle dependence of $\tilde{T}_v(\boldsymbol{r})$ and the interlayer potential difference Δ_z which is defined as

$$\Delta_z(\boldsymbol{r}) = \frac{\Delta_b(\boldsymbol{r}) - \Delta_t(\boldsymbol{r})}{2}. \tag{11}$$

Thus, in Fig. 4(a), we present the spatial distribution of $\Delta_z(\boldsymbol{r})$ at 3.89° and 2.00°. The primary contributions to Δ_z come from the ferroelectric potential $\tilde{V}_f$ and the piezoelectric potential $V_{p,t/b}$, which exhibit significant twist-angle-dependent competition [16], as detailed in Supplementary Note 3. This evolution is clearly reflected in the Fourier components of Δ_z, shown in Fig. 4(c). As θ decreases, the first harmonic $|\delta_z^1|$ drops rapidly and approaches zero near 1.5°, before rising again at smaller angles. This non-monotonic behavior arises from a reversal in the dominant contribution—from $V_{p,t/b}$ to $\tilde{V}_f$—in the MX/XM regions, resulting in a sign flip of Δ_z. Meanwhile, the third harmonic $|\delta_z^3|$ increases with decreasing
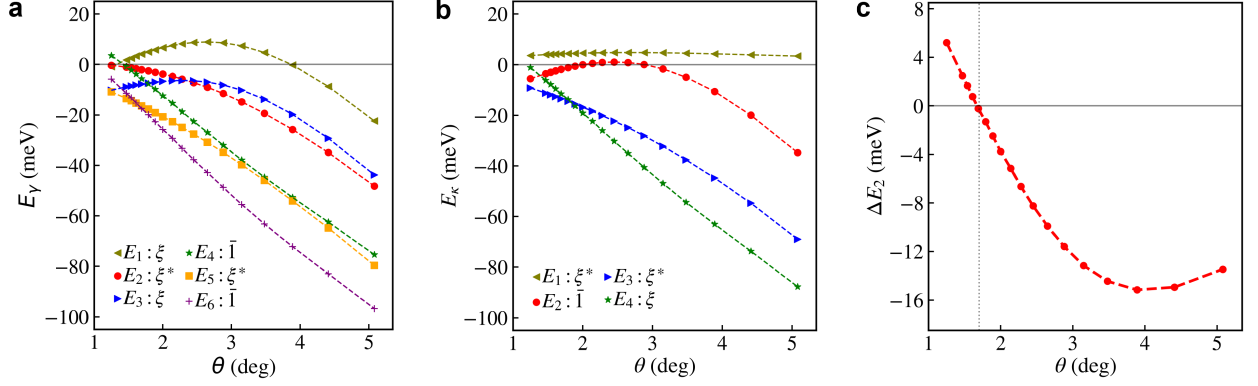
FIG. 5. **Perturbed band energies of tMoTe$_2$. a**, twist-angle dependence of the six perturbed eigenvalues at the γ point. The eigenvalues are labeled according to their spinful $\hat{C}_3$ eigenvalues: $\xi = e^{i\pi/3}$, $\xi^* = e^{-i\pi/3}$, and $\bar{1} = -1$. **b**, twist-angle dependence of the four perturbed eigenvalues at the κ point. **c**, twist-angle dependence of the second eigenvalue difference between the γ and κ points, defined as $\Delta E_2 = E_{\gamma 2} - E_{\kappa 2}$.

θ above $2.00°$ and then decreases at smaller angles. In particular, $|\delta_z^2|$ vanishes due to the preserved symmetry $\hat{C}_{2y}T$ of Eq. 8, where T denotes time-reversal symmetry and $\hat{C}_{2y}$ is the twofold rotation about the y axis.

Fig. 4(b) and (d) show the distributions and Fourier components of the interlayer tunneling $\tilde{T}_v(\boldsymbol{r})$, respectively. $\tilde{T}_v$ is primarily localized around the MM regions, while it vanishes near the MX/XM regions. As θ decreases from $3.89°$ to $2.00°$, the MM region shrinks, leading to a reduction in the first harmonic $|t_v^1|$. Meanwhile, the higher harmonics remain relatively small compared to $|t_v^1|$.

Next, we examine how the moiré potential terms influence the band energies. Since the topological phase transition and band flattening are mainly governed by Δ_z and $\tilde{T}_v$, we neglect the vector potentials $\boldsymbol{A}_{u,t/b}$ as well as the interlayer tunneling terms $\tilde{T}_{cv}$ and $\tilde{T}_{vc}$, whose effects are discussed in Supplementary Note 4. Figure 5(a) shows the θ dependence of the perturbed K-valley eigenvalues at the γ point, labeled by their spinful $\hat{C}_3$ eigenvalues. As θ decreases, we observe an inversion between $E_{\gamma 2}$ and $E_{\gamma 3}$ near $2.5°$, while $E_{\gamma 1}$ remains the highest in energy down to $1.5°$. Within the range of $1.5°$ to $2.5°$, $E_{\gamma 1}$ and $E_{\gamma 2}$ carry $\hat{C}_3$ eigenvalues of (ξ, ξ^*). Figure 5(b) presents the θ-dependence of the perturbed eigenvalues at the κ point. Here, $E_{\kappa 1}$ remains non-inverted with respect to the other eigenvalues as θ decreases, whereas $E_{\kappa 2}$ and $E_{\kappa 3}$ undergo an inversion below $1.5°$. Above $1.5°$, $E_{\kappa 1}$ and $E_{\kappa 2}$ carry $\hat{C}_3$ eigenvalues of $(\xi^*, \bar{1})$, respectively. Further, in the range of $1.6°$-$2.5°$, the first and second bands carry Chern numbers of $(+1, +1)$, as inferred from their $\hat{C}_3$ eigenvalues. These trends are consistent with both the continuum model and DFT results.

We then define $\Delta E_2 = E_{\gamma 2} - E_{\kappa 2}$ to measure the flatness of the second band. As shown in Fig. 5(c), at large angles, ΔE_2 is negative, while at small angles, it becomes

positive, crossing zero near $1.7°$. This behavior can be understood by using the following expressions of $E_{\gamma 2}$ and $E_{\kappa 2}$,

$$E_{\gamma 2} = E_{\text{kin}} + 2\delta_0^1 + |2t_v^1 + t_v^2|,$$
$$E_{\kappa 2} = E_{\text{kin}} - \delta_0^1 - \sqrt{3}\text{Im}[\delta_z^1], \qquad (12)$$

where E_{kin} denotes the kinetic energy. The strong θ dependence of ΔE_2 is dominated by the competition between $|t_v^1|$ and $|\delta_z^1|$, as both $|\delta_0^1|$ and $|t_v^2|$ exhibit only weak dependence on θ (see Fig. 4 and Supplementary Note 3). Notably, due to the $\hat{C}_{2y}T$ symmetry, δ_z^1 is purely imaginary, with $\text{Im}[\delta_z^1]$ remaining negative for $\theta_{\dot{\iota}}1.5°$. At large twist angles, $|\delta_z^1|_{\dot{\iota}}|t_v^1|$; conversely, at small angles, $|\delta_z^1|_{\dot{\iota}}|t_v^1|$ (see Fig. 4). As a result, ΔE_2 crosses zero at an intermediate θ. A similar trend is observed in tWSe$_2$, as illustrated in Supplementary Note 4, where ΔE_2 crosses zero at a slightly larger θ—consistent with DFT results. This resemblance stems from the similar θ-dependent lattice relaxations and moiré potentials in tMoTe$_2$ and tWSe$_2$.

In summary, we have developed a twist-angle transferable continuum model that comprehensively incorporates lattice relaxation effects as well as long-range ferroelectric and piezoelectric potentials in tMoTe$_2$ and tWSe$_2$. All model parameters are extracted from DFT band structures at a single twist angle ($3.89°$) and from monolayer TMD inputs. The model can be efficiently transferred to other twist angles using only moiré structural data obtained from MLFFs, eliminating the need for additional large-scale DFT calculations. Its transferability is demonstrated over the $2°$–$5°$ range, showing good agreement with DFT results in predicting both band dispersions and quantum geometries.

In previous continuum models, Δ_z and $\tilde{T}_v$ have been used to define the Skyrmion lattice [16, 25, 39, 40]. However, as illustrated in Fig. 4, both Δ_z and $\tilde{T}_v$ diminish near the MX/XM stacking regions at $2.00°$, leading to a

vanishing Skyrmion exchange field in those areas. This suggests that the adiabatic Skyrmion model may fail to capture the electronic behavior near this twist angle.

Using twist-angle-dependent moiré potentials, we identify the origin of the second flat Chern band near $2°$, arising when the interlayer potential difference becomes comparable to the interlayer tunneling. This finding provides a basis for searching for multiple flat Chern bands in other systems. As the model is structure-based, it also opens the possibility of exploring novel band geometric properties by designing specific lattice relaxation patterns [41–43]. The proposed framework is generalizable to other TMDs and can be extended to multilayer supermoiré structures. Looking ahead, the continuum model offers a promising basis for engineering novel electronic phases through strain, pressure, and twist angle, etc.

Acknowledgements

Author contributions

XWZ, TC, and DX conceived the project. XWZ carried out the construction of the continuum model and DFT calculations with assistance from KY, TC, and DX. CW performed the Wannier function calculations. XWZ, TC, and DX analyzed the results and wrote the paper with input from YK, CW, and XL.

Competing interests

The authors declare no competing interests.

Data availability

The fitted model parameters, Fourier components of the moiré potentials, and the neural network for the MLFFs have been deposited on GitHub. Additional data related to this paper are available from the corresponding authors upon request.

Corresponding authors: Ting Cao (tingcao@uw.edu); Di Xiao (dixiao@uw.edu)

[1] J. Cai, E. Anderson, C. Wang, X. Zhang, X. Liu, W. Holtzmann, Y. Zhang, F. Fan, T. Taniguchi, K. Watanabe, et al., Signatures of fractional quantum anomalous hall states in twisted mote2, Nature **622**, 63 (2023).

[2] Y. Zeng, Z. Xia, K. Kang, J. Zhu, P. Knüppel, C. Vaswani, K. Watanabe, T. Taniguchi, K. F. Mak, and J. Shan, Thermodynamic evidence of fractional chern insulator in moiré mote2, Nature **622**, 69 (2023).

[3] H. Park, J. Cai, E. Anderson, Y. Zhang, J. Zhu, X. Liu, C. Wang, W. Holtzmann, C. Hu, Z. Liu, et al., Observation of fractionally quantized anomalous hall effect, Nature **622**, 74 (2023).

[4] F. Xu, Z. Sun, T. Jia, C. Liu, C. Xu, C. Li, Y. Gu, K. Watanabe, T. Taniguchi, B. Tong, et al., Observation of integer and fractional quantum anomalous hall effects in twisted bilayer mote 2, Physical Review X **13**, 031037 (2023).

[5] B. A. Foutty, C. R. Kometter, T. Devakul, A. P. Reddy, K. Watanabe, T. Taniguchi, L. Fu, and B. E. Feldman, Mapping twist-tuned multiband topology in bilayer wse2, Science **384**, 343 (2024).

[6] K. Kang, B. Shen, Y. Qiu, Y. Zeng, Z. Xia, K. Watanabe, T. Taniguchi, J. Shan, and K. F. Mak, Evidence of the fractional quantum spin hall effect in moiré mote2, Nature **628**, 522 (2024).

[7] K. P. Nuckolls and A. Yazdani, A microscopic perspective on moiré materials, Nature Reviews Materials , 1 (2024).

[8] Z. Ji, H. Park, M. E. Barber, C. Hu, K. Watanabe, T. Taniguchi, J.-H. Chu, X. Xu, and Z.-X. Shen, Local probe of bulk and edge states in a fractional chern insulator, Nature **635**, 578 (2024).

[9] E. Anderson, J. Cai, A. P. Reddy, H. Park, W. Holtzmann, K. Davis, T. Taniguchi, K. Watanabe, T. Smolenski, A. Imamoğlu, et al., Trion sensing of a zero-field composite fermi liquid, Nature **635**, 590 (2024).

[10] E. Redekop, C. Zhang, H. Park, J. Cai, E. Anderson, O. Sheekey, T. Arp, G. Babikyan, S. Salters, K. Watanabe, et al., Direct magnetic imaging of fractional chern insulators in twisted mote2, Nature **635**, 584 (2024).

[11] H. Park, J. Cai, E. Anderson, X.-W. Zhang, X. Liu, W. Holtzmann, W. Li, C. Wang, C. Hu, Y. Zhao, et al., Ferromagnetism and topology of the higher flat band in a fractional chern insulator, Nature Physics , 1 (2025).

[12] Y. Wang, J. Choe, E. Anderson, W. Li, J. Ingham, E. A. Arsenault, Y. Li, X. Hu, T. Taniguchi, K. Watanabe, et al., Hidden states and dynamics of fractional fillings in tmote2 moir\'e superlattices, arXiv preprint arXiv:2502.21153 (2025).

[13] E. Thompson, K. T. Chu, F. Mesple, X.-W. Zhang, C. Hu, Y. Zhao, H. Park, J. Cai, E. Anderson, K. Watanabe, et al., Visualizing the microscopic origins of topology in twisted molybdenum ditelluride, arXiv preprint arXiv:2405.19308 (2024).

[14] Y. Xia, Z. Han, K. Watanabe, T. Taniguchi, J. Shan, and K. F. Mak, Superconductivity in twisted bilayer wse2, Nature **637**, 833 (2025).

[15] Y. Guo, J. Pack, J. Swann, L. Holtzman, M. Cothrine, K. Watanabe, T. Taniguchi, D. G. Mandrus, K. Barmak, J. Hone, et al., Superconductivity in 5.0° twisted bilayer wse2, Nature **637**, 839 (2025).

[16] X.-W. Zhang, C. Wang, X. Liu, Y. Fan, T. Cao, and D. Xiao, Polarization-driven band topology evolution in twisted mote2 and wse2, Nature Communications **15**, 4223 (2024).

[17] Y. Jia, J. Yu, J. Liu, J. Herzog-Arbeitman, Z. Qi, H. Pi, N. Regnault, H. Weng, B. A. Bernevig, and Q. Wu, Moiré fractional chern insulators. i. first-principles calculations and continuum models of twisted bilayer mote 2, Physical Review B **109**, 205121 (2024).

[18] N. Mao, C. Xu, J. Li, T. Bao, P. Liu, Y. Xu, C. Felser, L. Fu, and Y. Zhang, Transfer learning relaxation, electronic structure and continuum model for twisted bilayer mote2, Communications Physics **7**, 262 (2024).

[19] C. Wang, X.-W. Zhang, X. Liu, Y. He, X. Xu, Y. Ran, T. Cao, and D. Xiao, Fractional chern insulator in twisted bilayer mote 2, Physical Review Letters **132**, 036501 (2024).

[20] C.-E. Ahn, W. Lee, K. Yananose, Y. Kim, and G. Y. Cho, Non-abelian fractional quantum anomalous hall states and first landau level physics of the second moiré band of twisted bilayer mote 2, Physical Review B **110**, L161109 (2024).

[21] A. P. Reddy, N. Paul, A. Abouelkomsan, and L. Fu, Non-abelian fractionalization in topological minibands, Physical Review Letters **133**, 166503 (2024).

[22] C. Xu, N. Mao, T. Zeng, and Y. Zhang, Multiple chern bands in twisted mote 2 and possible non-abelian states, Physical Review Letters **134**, 066601 (2025).

[23] F. Chen, W.-W. Luo, W. Zhu, and D. Sheng, Robust non-abelian even-denominator fractional chern insulator in twisted bilayer mote2, Nature Communications **16**, 2115 (2025).

[24] C. Wang, X.-W. Zhang, X. Liu, J. Wang, T. Cao, and D. Xiao, Higher landau-level analogs and signatures of non-abelian states in twisted bilayer mote 2, Physical Review Letters **134**, 076503 (2025).

[25] F. Wu, T. Lovorn, E. Tutuc, I. Martin, and A. MacDonald, Topological insulators in twisted transition metal dichalcogenide homobilayers, Physical review letters **122**, 086402 (2019).

[26] S. J. Magorrian, V. Enaldiev, V. Zólyomi, F. Ferreira, V. I. Fal'ko, and D. A. Ruiz-Tijerina, Multifaceted moiré superlattice physics in twisted wse 2 bilayers, Physical Review B **104**, 125440 (2021).

[27] H. Tang, S. Carr, and E. Kaxiras, Geometric origins of topological insulation in twisted layered semiconductors, Physical Review B **104**, 155415 (2021).

[28] Y. Zhang, H. Pi, J. Liu, W. Miao, Z. Qi, N. Regnault, H. Weng, X. Dai, B. A. Bernevig, Q. Wu, et al., Universal moir\'e-model-building method without fitting: Application to twisted mote _2 and wse _2, arXiv preprint arXiv:2411.08108 (2024).

[29] K.-A. N. Duerloo, M. T. Ong, and E. J. Reed, Intrinsic piezoelectricity in two-dimensional materials, The Journal of Physical Chemistry Letters **3**, 2871 (2012).

[30] V. Enaldiev, V. Zólyomi, C. Yelgel, S. Magorrian, and V. Fal'Ko, Stacking domains and dislocation networks in marginally twisted bilayers of transition metal dichalcogenides, Physical review letters **124**, 206101 (2020).

[31] M. Wu and J. Li, Sliding ferroelectricity in 2d van der waals materials: Related physics and future opportunities, Proceedings of the National Academy of Sciences **118**, e2115703118 (2021).

[32] X. Wang, K. Yasuda, Y. Zhang, S. Liu, K. Watanabe, T. Taniguchi, J. Hone, L. Fu, and P. Jarillo-Herrero, Interfacial ferroelectricity in rhombohedral-stacked bilayer transition metal dichalcogenides, Nature nanotechnology **17**, 367 (2022).

[33] R. Bistritzer and A. H. MacDonald, Moiré bands in twisted double-layer graphene, Proceedings of the National Academy of Sciences **108**, 12233 (2011).

[34] J. Jung, A. Raoux, Z. Qiao, and A. H. MacDonald, Ab initio theory of moiré superlattice bands in layered two-dimensional materials, Physical Review B **89**, 205414 (2014).

[35] V. Crépel, N. Regnault, and R. Queiroz, Chiral limit and origin of topological flat bands in twisted transition metal dichalcogenide homobilayers, Communications Physics **7**, 146 (2024).

[36] L. Balents, General continuum model for twisted bilayer graphene and arbitrary smooth deformations, SciPost Physics **7**, 048 (2019).

[37] M. Cazalilla, H. Ochoa, and F. Guinea, Quantum spin hall effect in two-dimensional crystals of transition-metal dichalcogenides, Physical review letters **113**, 077201 (2014).

[38] S. Fang, S. Carr, M. A. Cazalilla, and E. Kaxiras, Electronic structure theory of strained two-dimensional materials with hexagonal symmetry, Physical Review B **98**, 075106 (2018).

[39] N. Morales-Durán, N. Wei, J. Shi, and A. H. MacDonald, Magic angles and fractional chern insulators in twisted homobilayer transition metal dichalcogenides, Physical Review Letters **132**, 096602 (2024).

[40] J. Shi, N. Morales-Durán, E. Khalaf, and A. H. MacDonald, Adiabatic approximation and aharonov-casher bands in twisted homobilayer transition metal dichalcogenides, Physical Review B **110**, 035130 (2024).

[41] M. Van Winkle, I. M. Craig, S. Carr, M. Dandu, K. C. Bustillo, J. Ciston, C. Ophus, T. Taniguchi, K. Watanabe, A. Raja, et al., Rotational and dilational reconstruction in transition metal dichalcogenide moiré bilayers, Nature Communications **14**, 2989 (2023).

[42] L. G. Pimenta Martins, D. A. Ruiz-Tijerina, C. A. Occhialini, J.-H. Park, Q. Song, A.-Y. Lu, P. Venezuela, L. G. Cançado, M. S. Mazzoni, M. J. Matos, et al., Pressure tuning of minibands in mos2/wse2 heterostructures revealed by moiré phonons, Nature Nanotechnology **18**, 1147 (2023).

[43] K. X. Nguyen, Y. Jiang, C.-H. Lee, P. Kharel, Y. Zhang, A. M. van der Zande, and P. Y. Huang, Achieving sub-0.5-angstrom–resolution ptychography in an uncorrected electron microscope, Science **383**, 865 (2024)